

PAPER • OPEN ACCESS

Effect of edge ion temperature on the divertor tungsten sputtering in WEST

To cite this article: Y. Li et al 2023 Nucl. Fusion 63 026019

View the <u>article online</u> for updates and enhancements.

You may also like

- Experimental investigation on divertor tungsten sputtering with neon seeding in ELMy H-mode plasma in EAST tokamak Dawei Ye, , Fang Ding et al.
- The geometry of the ICRF-induced wave—SOL interaction. A multi-machine experimental review in view of the ITER operation

L. Colas, G. Urbanczyk, M. Goniche et al.

- EMC3-EIRENE modelling of tungsten behavior under resonant magnetic perturbations on EAST: Effects of tungsten sputtering and impurity screening S Y Dai, H M Zhang, B Lyu et al. Nucl. Fusion 63 (2023) 026019 (10pp)

Effect of edge ion temperature on the divertor tungsten sputtering in WEST

Y. Li¹, N. Fedorczak^{2,*}, G.S. Xu^{1,*}, Y. Liang³, S. Brezinsek³, J. Morales² and The WEST Team

E-mail: Nicolas.FEDORCZAK@cea.fr and gsxu@ipp.ac.cn

Received 27 July 2022, revised 15 December 2022 Accepted for publication 19 December 2022 Published 3 January 2023



Abstract

The influence of upstream ion temperature in the scrape-off layer (SOL) on the tungsten (W) sputtering in the divertor is studied in the WEST tokamak. For an almost constant power into the SOL, the upstream ion temperature and its ratio over the electron temperature gradually increase with the decrease of electron density in the SOL. This increment is observed to enhance the energy transfer from ions to electrons. This increases the downstream electron temperature and by coupling of electrons and ions, the impact energy of ions causing W sputtering in the divertor. This enhancement mechanism may become crucial to sputtering the W material for high upstream T_i/T_e ratio since the impact energy of ions in the divertor would increase accordingly.

Keywords: tungsten sputtering, ion temperature, energy transfer, upstream and downstream electron temperature ratio, SOL

(Some figures may appear in colour only in the online journal)

1. Introduction

The realization of fusion power faces a number of large challenges. One of them is the plasma-wall interaction [1], where the outflux of the hot and dense plasma continuously bombards the so-called plasma-facing components in the divertor area which is designed to handle the power and particle exhaust. Tungsten (W) was selected as the divertor plasmafacing material in current tokamaks like JET [2], ASDEX Upgrade (AUG) [3] and W (tungsten) Environment in Steadystate Tokamak (WEST) [4] and in the International Thermonuclear Experimental Reactor (ITER) [5] to maximize the

Original content from this work may be used under the terms of the Creative Commons Attribution 4.0 licence. Any further distribution of this work must maintain attribution to the author(s) and the title of the work, journal citation and DOI.

operational space and ensure integrity of components in the harsh environment.

Unlike graphite or other carbon-based materials, W can be only eroded by physical sputtering [6]. And its threshold energy for the impacting particles with low mass number is much higher [7]. For example, the hydrogen and deuterium particles require more than 200 eV impact energy $(E_{\rm i} = 3T_{\rm ed} + 2T_{\rm id})$ to sputter W, where $T_{\rm ed}$ and $T_{\rm id}$ are the downstream electron and ion temperature, respectively. In the case of steady-state operation in L-mode, W is sputtered by intrinsic or extrinsic impurities [3, 8–10]. While in H mode, due to edge-localized-mode eruption, hot ions (~keV) transport from the pedestal to the divertor, can directly erode W [11-14].

When the plasma is still attached, the downstream plasma parameters in the divertor, including the ion impact energy, is correlated with the upstream plasma parameters of the scrapeoff-layer (SOL) region [15]. Due to the lack of direct ion temperature measurement at the SOL, the study of W erosion and transport is usually limited to optical emission spectroscopy

¹ Institute of Plasma Physics, Chinese Academy of Sciences, Hefei 230031, China

² CEA, IRFM, F-13108 Saint-Paul-lez-Durance, France

³ Forschungszentrum Jülich GmbH, Institut für Energie- und Klimaforschung—Plasmaphysik, Partner of the Trilateral Euregio Cluster (TEC), 52425 Jülich, Germany

Authors to whom any correspondence should be addressed. See (http://west.cea.fr/WESTteam) for The WEST Team

and the electron temperature measurement [16]. The effect of the ion temperature is barely considered in the theoretical simulation [17]. While in some experiments, the upstream ion temperature $T_{\rm iu}$ has been measured to be much larger than the upstream electron temperature $T_{\rm eu}$, and their ratio $\tau_{\rm u} = T_{\rm iu}/T_{\rm eu}$ is strongly dependent on the plasma density and collisionality [18–21]. This implies that the effect of upstream ion temperature may play indirectly an important role on the W erosion in the downstream area of the divertor.

In this paper, we present that the W sputtering yield in the downstream area of the divertor is correlated with the upstream ion temperature. An energy transfer from ions to electrons with value comparable with the perpendicular electron energy transport would potentially increase the downstream electron temperature.

This paper is organized as follows. Section 2 introduces the diagnostic layout and shows the experimental results. Section 3 shows the dependence of divertor W sputtering on the upstream and downstream plasma parameters. Section 4 discusses the relation of E_i with the upstream parameters and an enhancement of divertor electron temperature due to energy transfer from ions to electrons in the studied range of divertor conditions. Finally the conclusion is made in section 5.

2. Experimental setup

WEST is a superconducting tokamak with major radius 2.5 m and minor radius 0.5 m [4], aiming to test the ITER divertor technology with W monoblocks in a steady state tokamak environment. The remaining plasma facing components, including the upper divertor, use W coating on graphite. Its superconducting coil system, including toroidal and poloidal coil systems, are succeeded from the Tore Supra tokamak, which have achieved steady state long pulse operation [22].

A series of discharges in deuterium are conducted with the retarding field analyzer (RFA) operation. Twelve cases for nine discharges with similar magnetic geometry and plasma operation conditions are analyzed in this paper. Among these discharges, the plasma current I_p is 0.5 MA, and the toroidal magnetic fields is 3.76 T at $R_0 = 2.42$ m, resulting in q95 to be 4.4. The auxiliary heating power is provided by lower hybrid wave heating with 4 MW. The power entering the SOL after subtracting the divertor radiation is almost constant \sim 1.85 MW. A poloidal cross section with two almost identical magnetic geometries within the dataset and the diagnostic layout are shown in figure 1. The upstream plasma parameters including the upstream ion temperature are measured by the RFA and Langmuir probes mounted at the reciprocating probe system located at the outer top of the device, thus relatively close to the stagnation point [23]. The downstream plasma parameters are measured by the divertor Langmuir probe array [24] where the probe location is shown in figure 1 with green dots. The W erosion in the divertor is related to the divertor WI brightness at a wavelength 400.9 nm and measured by visible spectroscopy [25] where the line of sight (LOS) position is shown as purple lines in figure 1. The two magnetic geometries as seen in figure 1 are from discharges #55 067 (solid line)

WEST: [55067(solid) 55070(dashed)]@20s

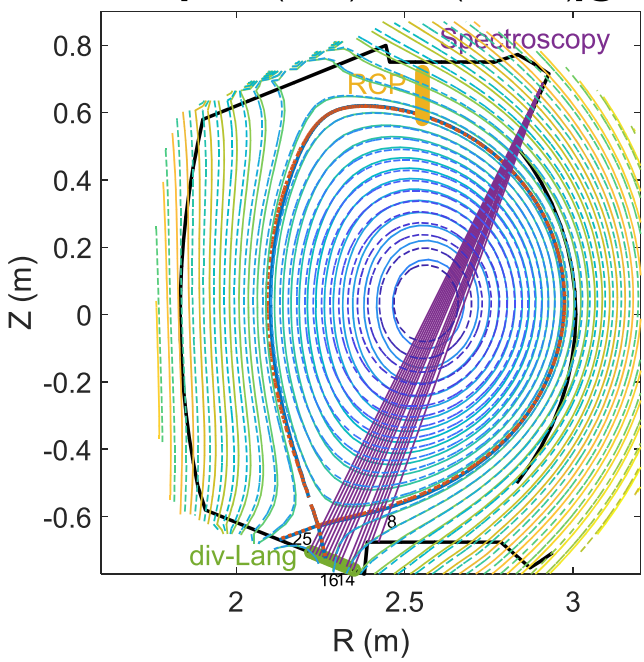


Figure 1. WEST magnetic configuration of discharges #55 067 (solid line) and #55 070 (dashed line) at 20 s when the RFA is plunged into the plasma. The last closed flux surfaces for these two discharges are shown as blue solid line and red dashed line, respectively. The yellow bar is the reciprocating probe movement path. The green dots show the divertor Langmuir probe array location. The purple line array is the field of view of the visible Spectroscopy.

and #55 070 (dashed line) and calculated by Newton direct and Inverse Computation for Equilibrium (NICE) code [26]. Their waveforms of the main plasma parameters are shown in figure 2.

As can be seen in figure 2, the plasmas in both discharges are operated steady state after the current flat top is built. The central line integrated density $n_{\rm el}$, lower hybrid wave heating power P_{LH} , ohmic heating power P_{ohm} , bulk plasma radiation P_{bulk} and divertor plasma radiation $P_{\text{div,low}}$ are almost identical in both discharges. At the flat-top region, the main plasma parameters for both discharges are fixed at $I_p = 0.5$ MA, $n_{\rm el} = 4 \times 10^{19}$ m⁻², $P_{\rm LH} = 4$ MW, $P_{\rm bulk} = 2$ MW. The D₂ gas is first prefilled from the top of the chamber on the low field side and then fueled from the midplane in the vicinity of one ion cyclotron resonance heating (ICRH) antenna to sustain a target plasma density. Though the central line integrated density is almost identical in both discharges, the gas puffing rate in #55 067 is much higher than that in #55 070. This may be caused by different wall outgassing conditions. The core electron temperature measured by electron cyclotron emission (ECE) is observed to be slightly larger in #55 070 than that in #55 067 at the steady state regime.

Due to different D_2 gas puffing rate, the divertor plasma is also affected and shown in figure 3. In this figure, the divertor plasma parameters shown at sub-figures 3(a)–(d) are measured by the divertor Langmuir probe array and are located near the outer strike point (OSP). More gas fuelling is

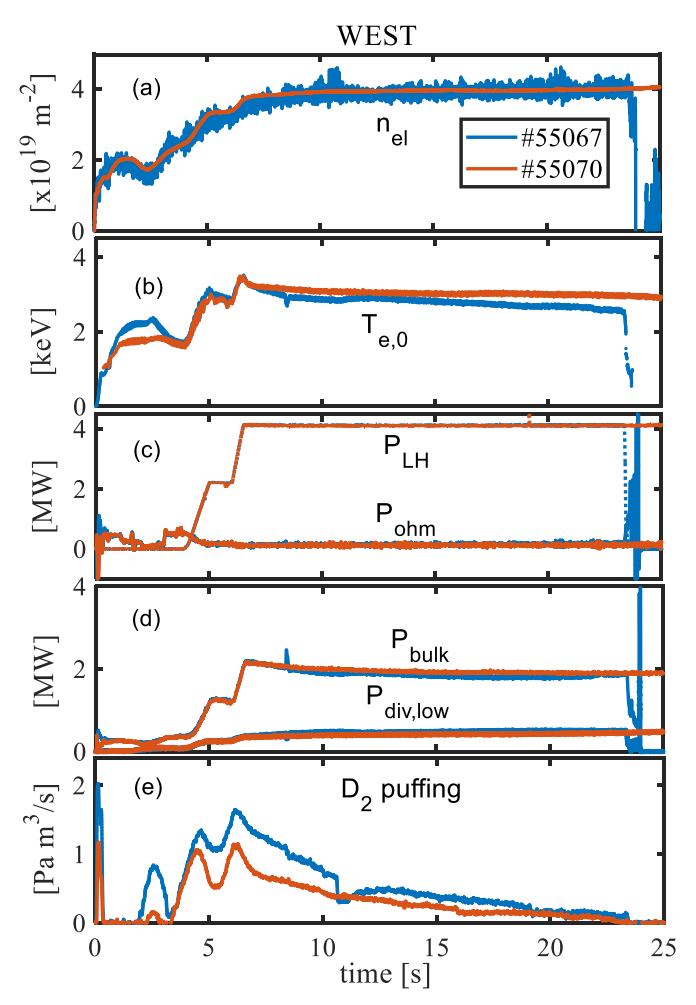


Figure 2. Evolution of (*a*) central line integrated density $n_{\rm el}$, (*b*) core electron temperature $T_{\rm e,0}$, (*c*) lower hybrid wave heating power $P_{\rm LH}$ and ohmic heating power $P_{\rm ohm}$, (*d*) bulk plasma radiation $P_{\rm bulk}$ and divertor plasma radiation $P_{\rm div,low}$, (*e*) gas puffing rate for pulse #55 067 (blue) and #55 070 (red). Note that the RFA and Langmuir probes are plunged at 20 s.

correlated with larger parallel ion saturated current density $(j_{\text{sat},\parallel})$ and plasma density (n_{ed}) near the strike point in #55 067 than that in #55 070 as seen in figures 3(a) and (b). As the time increases, their increment become larger. This leads to a cooler plasma near the divertor, i.e. lower plasma temperature in #55 067. From \sim 12 s, the downstream electron temperature at both discharges gradually decrease as the plasma density increases. Note that the neutral particle ionization is negligible to cool the plasma. Assume that the average loss per ionization is \sim 30 eV, by multiplying it with the gas puffing rate, the electron energy cost to ionize all of the puffed neutrals is 2.3 kW. This value is much smaller than P_{SOL} . Cooler plasma has led to lower W sputtering in #55 067 than in #55 070 as shown in figures 3(e) and (f), where the W sputtering flux $\Gamma_{W,\perp}$ and yields $Y_W = \Gamma_{W,\perp}/\Gamma_{D,\perp}$ are for WI lines at $\lambda = 400.9$ nm near the OSP, $\Gamma_{D,\perp}$ is the perpendicular deuterium particle flux near the OSP. The inverse photon efficiencies or so-called effective S/XB values are calculated based on

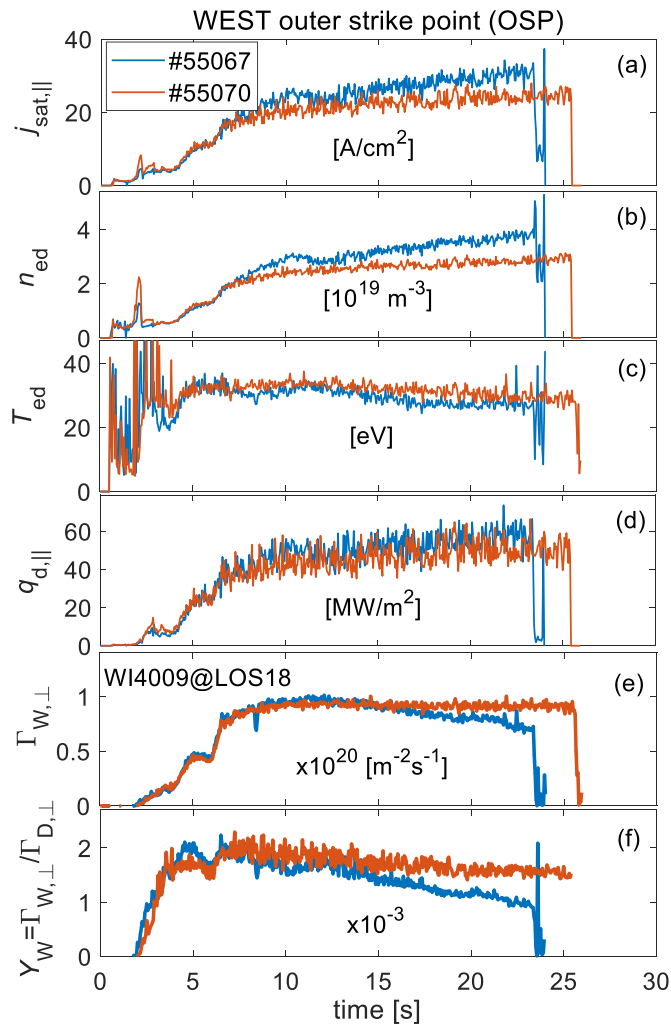


Figure 3. Evolution of divertor parallel ion saturated current $j_{\text{sat},\parallel}(a)$, downstream electron density $n_{\text{ed}}(b)$ and temperature $T_{\text{ed}}(c)$, parallel heat flux $q_{\text{d},\parallel}(d)$ near the outer strike point measured by divertor Langmuir probes, and W sputtering flux $\Gamma_{\text{W},\perp}(e)$ and yields $Y_{\text{W}}(f)$ measured by Spectroscopy with the LOS18 channel at a wavelength $\lambda=400.9$ nm for pulse #55 067 (blue) and #55 070 (red).

equation S/XB($T_{\rm e}$) = 53.63 – 56.07 × exp (-0.045 × $T_{\rm e}$ [eV]) as shown in [27]. After multiplying the S/XB coefficient, the W atom influx $\Gamma_{\rm W,\perp}$ is calculated and used to estimate the effective W sputtering yield $Y_{\rm W} = \Gamma_{\rm W,\perp}/\Gamma_{\rm D,\perp}$.

However, the divertor plasma remains in the full ionizing regime with peak electron temperatures at the strike line above 25 eV. The corresponding impact energy for D would be \sim 125 eV, thus, below the W sputtering threshold. Therefore, the W sputtering is determined by impurities in the plasma. In WEST, the main impurities in the divertor are boron (B) and carbon (C), while the oxygen (O) impurity influx is an order of magnitude smaller as seen in figure 4. Their particle concentrations in the divertor, estimated by comparing with the D ion particle flux are roughly 0.8% for B, 0.4% for C and 0.03% for O. In addition, since the impurity concentration in

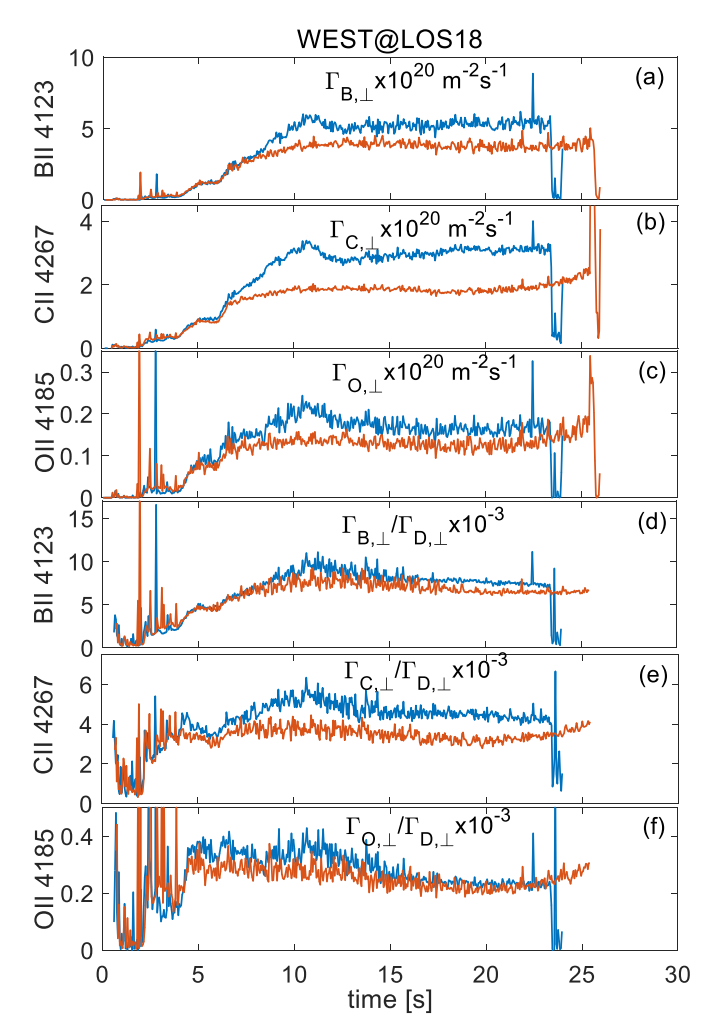


Figure 4. Evolution of ion flux of (a) boron $\Gamma_{B,\perp}$ at a wavelength $\lambda=412.3$ nm, (b) carbon $\Gamma_{C,\perp}$ at a wavelength $\lambda=426.7$ nm, (c) oxygen $\Gamma_{O,\perp}$ at a wavelength $\lambda=418.5$ nm, and impurity concentration of (d) boron $\Gamma_{B,\perp}/\Gamma_{D,\perp}$, (e) carbon $\Gamma_{C,\perp}/\Gamma_{D,\perp}$, (f) oxygen $\Gamma_{O,\perp}/\Gamma_{D,\perp}$ measured by Spectroscopy near the outer strike point with the LOS18 channel for pulse #55 067 (blue) and #55 070 (red).

the steady state regime is much lower in #55 070 than that in #55 067, the larger W sputtering yield in #55 070 is attributed to higher impact energy of impurities, i.e. hotter divertor plasma in #55 070 than that in #55 067.

In these two discharges, the W sputtering yield $Y_{\rm W,\perp}$ is also shown as functions of the plasma parameters $n_{\rm ed}$, $\Gamma_{\rm ed}$, $\Gamma_{\rm D,\perp}$ and $q_{\rm d,\parallel}$ at the OSP as seen in figure 5, where the data is selected between 13 and 22 s at the flat top of discharges #55 067 and #55 070. For both discharges, $Y_{\rm W,\perp}$ gradually decreases with $n_{\rm ed}$, $\Gamma_{\rm D,\perp}$ and $q_{\rm d,\parallel}$, and increases with $T_{\rm ed}$. It should be stated that the plasma parameters, such as $n_{\rm ed}$ and $T_{\rm ed}$, are coupled in these experiments. It is not that $n_{\rm ed}$ is constant and $T_{\rm ed}$ can be increased or vice versa. Since the W sputtering is strongly correlated with the impact energy of hydrogen isotopes and impurity particles [8], it is reasonable to imply that the tendency between $Y_{\rm W}$ and $n_{\rm ed}$ is caused by the variation of $T_{\rm ed}$.

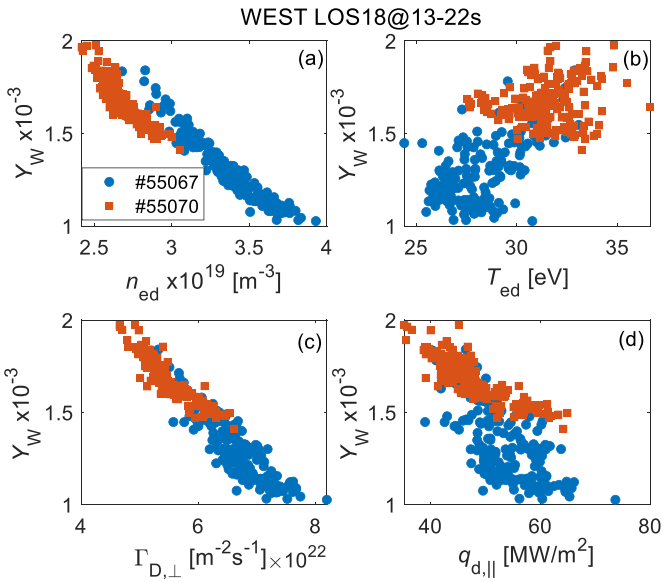


Figure 5. W sputtering yield as functions of (a) downstream electron density, (b) downstream electron temperature $T_{\rm ed}$, (c) perpendicular particle flux $\Gamma_{\rm D,\perp}$, and (d) parallel heat flux $q_{\rm d,\parallel}$ near the outer strike point for pulse #55 067 (blue circle) and #55 070 (red square).

3. Dependence of divertor W sputtering on upstream and downstream plasma parameters

3.1. Measurement of upstream and downstream plasma profiles

For discharges of #55 067 and #55 070, the upstream RFA and Langmuir probes are plunged into the plasma after 20 s long pulse operation. The measured profiles of upstream ion temperature $T_{\rm e}$ and density $n_{\rm e}$ are shown in figure 6, and the movement position of these two probes are shown in figure 7(h). The fitting curves for each profile in figure 6 is based on the exponential function. The result shows that the plasma density in the SOL in #55 070 is \sim 30% lower than that in #55 067. This induces much higher $\tau_{\rm u}$ in lower plasma density discharge #55 070, where the $T_{\rm i}$ ($T_{\rm e}$) profiles are slightly higher (lower) than those in discharge #55 067.

Lower gas puffing also accompanied smaller downstream plasma density and parallel particle flux in #55 070 than in #55 067 as seen in figures 7(a) and (c) and the corresponding temporal evolution at strike point in figures 7(e) and (g) measured by the divertor Langmuir probe array. In this figure, the downstream plasma parameter profiles are shown in figures 7(a)—(d) for time slices of 20.30 s and 20.35 s during the upstream RFA and Langmuir probe movement period, and the temporal evolutions shown in figures 7(e)—(h) are corresponding to the plasma parameters at the strike point. In contrast, the downstream electron temperature is higher in #55 070 than in #55 067 as seen in figures 7(b) and (f), where T_e is increased for \sim 20% near the strike point. Despite that the

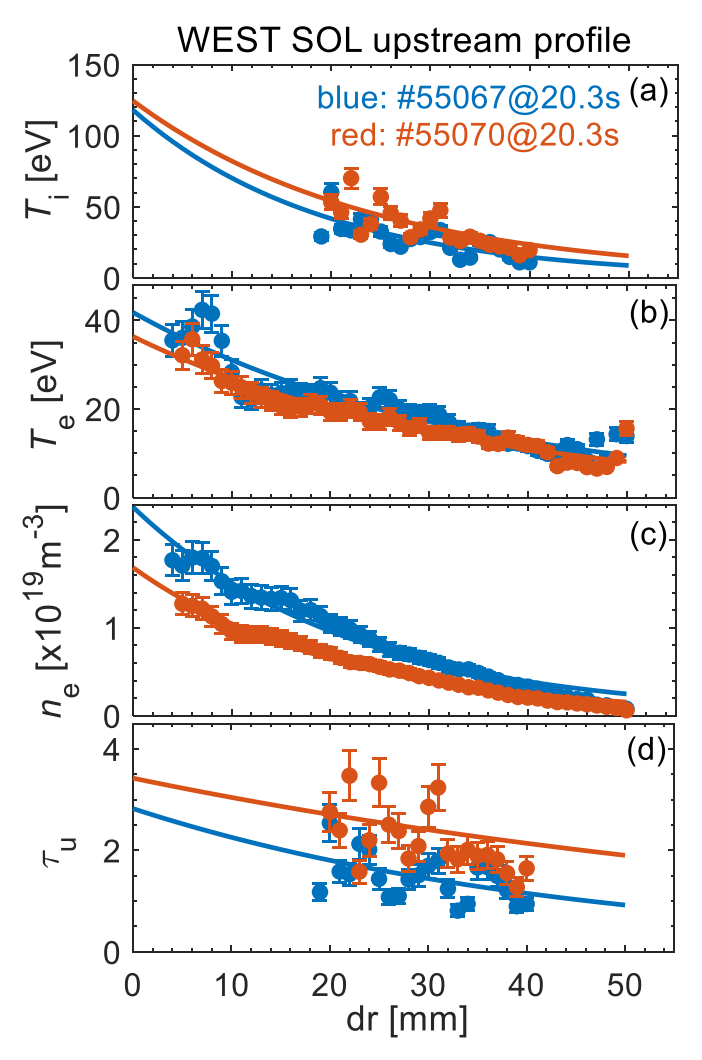


Figure 6. Upstream profiles of (a) T_i , (b) T_e , (c) n_e and (d) τ_u measured by RFA and Langmuir probes. The curves in each subfigure are obtained by exponentially fitting the measurement profiles. Note that the error bars of the measurements of the upstream RFA and Langmuir probe are set to be 20%. The reciprocating probe measurements are obtained by fitting the corresponding single I–V characteristic every 2 ms.

divertor electron density and temperature were changed, the parallel heat flux are still almost identical for both discharges as seen in figure 7(h). Note that the divertor plasma parameters are perturbated largely at the strike point, especially in #55 070. This leads to the parameters of $T_{\rm e}$, $j_{\rm sat,\parallel}$, and $q_{\rm d,\parallel}$ at the strike point varied significantly from 20.30 s to 20.35 s.

By means of the measurement by divertor Langmuir probe array and spectroscopy, the spatio and temporal evolution of W sputtering flux and yield are shown in figure 8, where figures 8(a)–(d) are the profiles of WI photon influx, W atom flux, D atom flux and W sputtering yield, respectively. Figures 8(e)–(h) show the temporal evolution of these parameters at the strike point. Though the particle flux impacting the W target is higher in #55 067 than in #55 070, the WI photon influx measured by the visible spectroscopy shows almost identical profiles in both discharges and even higher value in #55 070 near the strike point as shown in figures 8(a)

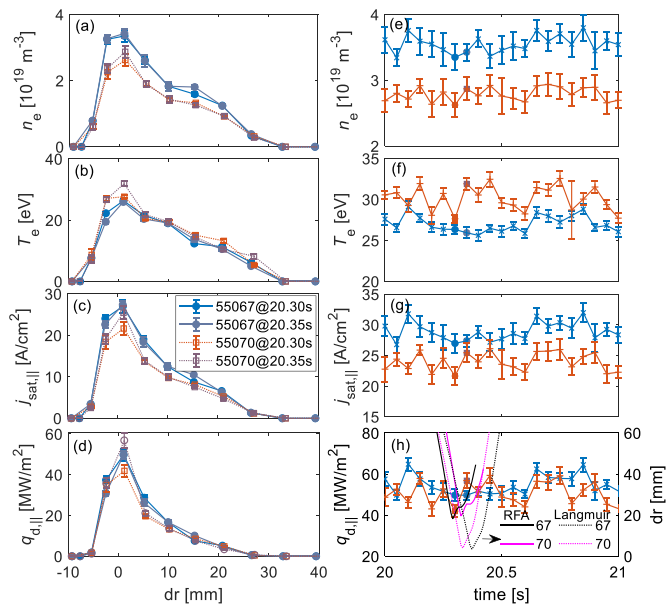


Figure 7. Downstream profiles of (a) n_e , (b) T_e , (c) $j_{\text{sat},\parallel}$, (d) $q_{\text{d},\parallel}$ measured by outer-lower divertor Langmuir probe array, and temporal evolution of (e) n_e , (f) T_e , (g) $j_{\text{sat},\parallel}$, (h) $q_{\text{d},\parallel}$ at the outer strike point. The upstream probe movements are shown in sub-figure (h) with solid line for RFA and dot line for Langmuir probe. '67' with black color and '70' with magenta color are corresponding to discharge #55 067 and #55 070, respectively. The time slices of 20.30 s and 20.35 s are also covered on the temporal evolution subfigures. Note that the error bars of the measurement of the downstream Langmuir probe array are from the least square fit of the I–V characteristic averaged over 50 ms in which each I–V characteristic is 4 ms.

and (e). After transforming the W photon influx to the W sputtering yield by multiplying the S/XB coefficient, $\Gamma_{W,\perp}$ at the strike point is clearly much higher in #55 070 than in #55 067 as shown in figure 8(f). After dividing by the perpendicular deuterium particle flux as shown in figures 8(c) and (g), the Y_W profile and its evolution at the strike point are much higher in #55 070 than that in #55 067 as shown in figures 8(d) and (h). In the strike point position, $Y_{\rm W}$ increases for roughly 30%. This could be easily understood since the ion impact energy is proportional to the downstream electron temperature. The strange increase of $Y_{\rm W}$ for dr > 20 mm is probably caused by the exponential decay of $\Gamma_{D,\perp}$ at this region which cannot properly reflect the light impurities concentration since W is preferably sputtered by the impurities such as B, C or O ions in the order of a few % [28]. Near the strike point, $Y_{\rm W}$ normalized by D+ could still be assumed to behave the same way as the impurity concentration. Therefore, the following statistic only focuses on the $Y_{\rm W}$ evolution near the OSP position.

3.2. Dependence of SOL plasma parameters on upstream electron density

For fixed $P_{SOL} \sim 1.85$ MW and lower hybrid current drive (LHCD) only discharges, changing the SOL plasma density has affected the upstream and downstream parameters, which in turn affect the divertor W sputtering. Figure 9 shows

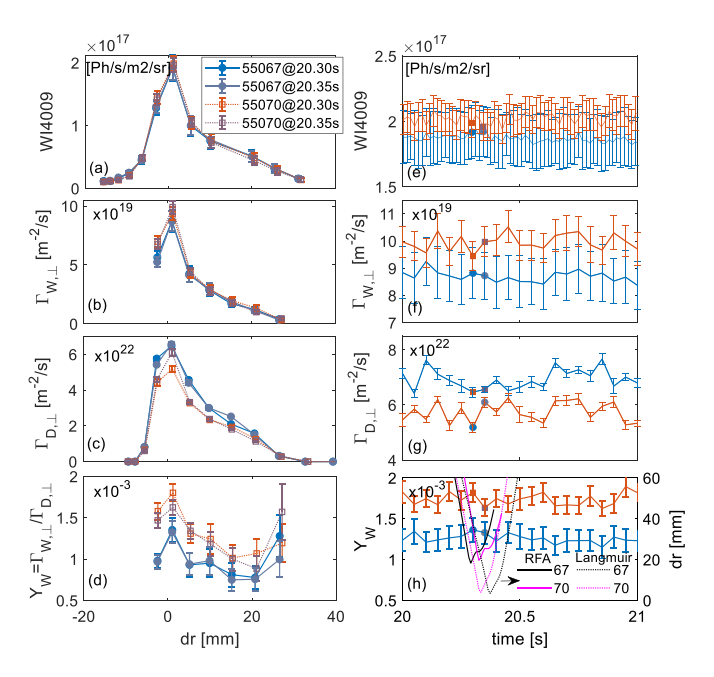


Figure 8. Downstream profiles of (a) WI lines at $\lambda = 400.9$ nm, (b) $\Gamma_{\rm W,\perp}$, (c) $\Gamma_{\rm D,\perp}$, (d) $Y_{\rm W}$ at outer-lower divertor, and temporal evolution of (e) WI lines at $\lambda = 400.9$ nm, (f) $\Gamma_{\rm W,\perp}$, (g) $\Gamma_{\rm D,\perp}$, (h) $Y_{\rm W}$ at the outer strike point.

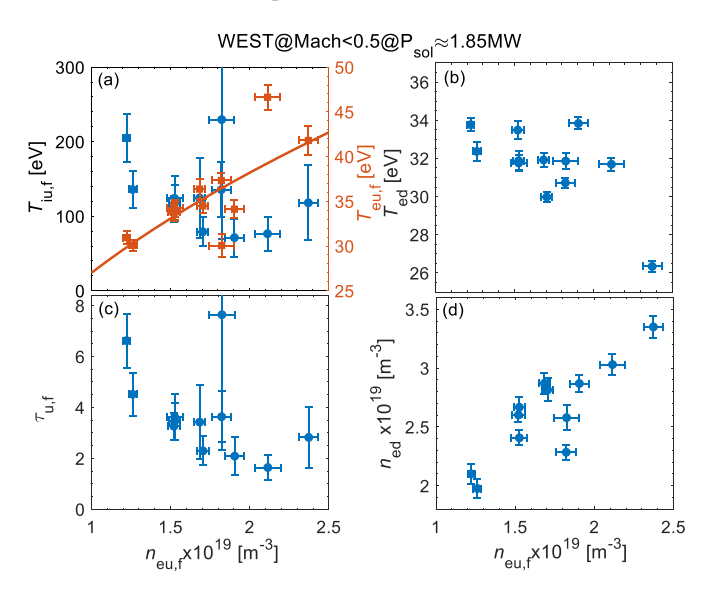


Figure 9. Dependence of (a) $T_{\rm iu,f}$ and $T_{\rm eu,f}$, (b) $T_{\rm ed}$, (c) $\tau_{u,f}$ and (d) $n_{\rm ed}$ on the upstream electron density, $n_{\rm eu,f}$, where the upstream plasma parameters are located near the separatrix and the downstream plasma parameters are located near the outer-lower strike point. The red curve in subfigure (a) represents the function $T_{\rm eu,f}=27\sqrt{n_{\rm eu,f}}$.

the SOL plasma parameters as a function of the upstream plasma density for 12 cases with the RFA operation in nine discharges. As can be seen, the parameters of $T_{\mathrm{iu},f}$ and $\tau_{u,f}$ roughly decrease with the increase of n_{eu} , where the subscript 'f' denotes that the relevant value is extrapolated but not measured. n_{ed} and $T_{\mathrm{eu},f}$ gradually increase with n_{eu} . These trends are consistent with the measurement carried out in the limiter plasma of Tore Supra, except that T_{eu} gradually decreases with the increased n_{el} in Tore Supra [18]. In addition, a tendency

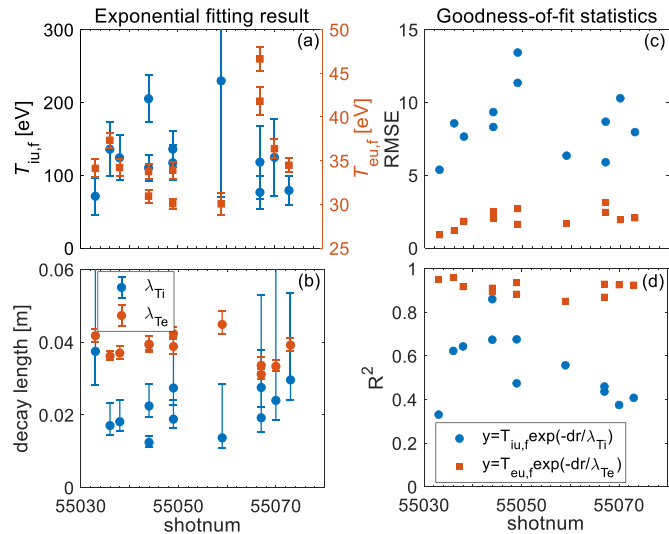


Figure 10. Exponential fitting result of (a) extrapolated ion and electron temperature at separatrix, $T_{\text{iu},f}$ and $T_{\text{eu},f}$, and (b) ion and electron temperature decay length, λ_{Ti} and λ_{Te} . Goodness-of-fit statistics of (c) Root mean squared error (RMSE) and (d) coefficient of determination, R^2 .

for $T_{\rm eu} \propto n_{\rm eu}^{1/2}$ was found to hold, not just at the separatrix but across the SOL of JET and Alcator C-Mod for the high recycling (conduction limited) divertor [29].

Note that the upstream parameters are located near the separatrix, and the downstream parameters are located near the outer-lower strike point. $T_{\text{iu},f}$ is extrapolated by exponentially fitting the measured points which is usually 2 cm away from the separatrix. This causes a larger uncertainty of $T_{\text{iu},f}$ near the separatrix, and leads to some distorted $T_{\text{iu},f}$ extrapolation points and the calculated $\tau_{u,f}$. The fitting result, including parameters of $T_{\text{iu},f}$, $T_{\text{eu},f}$, λ_{Ti} and λ_{Te} , and the goodness-of-fit statistics are shown in figure 10. Comparing with the electron temperature fitting, we can see that the ion temperature fitting behaves much larger root mean squared error and worse coefficient of determination ($R^2 \sim 0.5$), implying a much larger error bar in the $T_{\text{iu},f}$ extrapolation.

3.3. Dependence of W sputtering yield on SOL plasma parameters

The dependence of $Y_{\rm W}$ on the downstream plasma parameters in the dataset of these 12 cases is similar with the relation in figure 5 and not shown again. $Y_{\rm W}$ is also observed to gradually decrease with the increase of $n_{\rm ed}$, $\Gamma_{\rm D, \perp}$, and $q_{\rm d, \parallel}$, with $T_{\rm ed}$. This result is consistent with the observation in other devices [12], where increasing the downstream plasma density would usually cool down the plasma, and then decreases the impacted ion energy.

Because the downstream plasma parameters are determined by the upstream ones, $Y_{\rm W}$ also shows strongly correlation with the upstream plasma parameters. As seen in figure 11, $Y_{\rm W}$ is positively proportional with $T_{\rm iu,f}$ and $\tau_{u,f}$ when $\tau_{u,f} < 4$, and is inversely proportional with $n_{\rm eu,f}$. In contrast with the relation of $Y_{\rm W}$ with $T_{\rm ed}$, $Y_{\rm W}$ gradually decreases with the

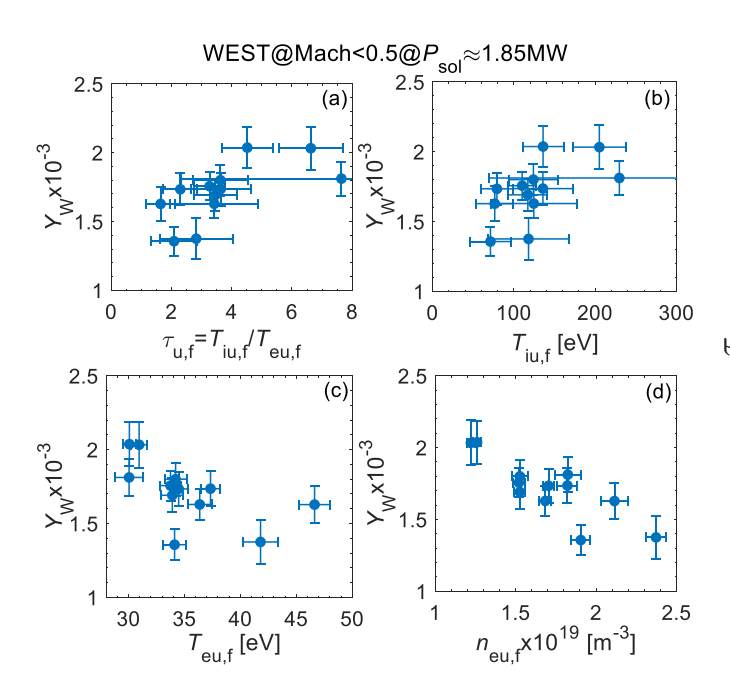


Figure 11. Effective W sputtering yield located near the outer-lower strike point as functions of (a) $\tau_{u,f}$, (b) $T_{\text{iu},f}$, (c) $T_{\text{eu},f}$ and (d) $n_{\text{eu},f}$ near the separatrix.

increase of $T_{\mathrm{eu},f}$. These opposite dependencies of Y_W on T_{ed} and $T_{\mathrm{eu},f}$ imply that the energy transfer from ions to electrons occurred in the SOL has enhanced the downstream electron temperature. Note that some scattering points with $\tau_{u,f} > 4$ are corresponding to $T_{\mathrm{iu},f} > 200$ eV. These high values may be caused by the ion temperature extrapolation method as shown in figure 10.

4. Enhancement of divertor electron temperature due to energy transfer from ions to electrons

4.1. Estimation of energy transfer from ions to electrons

When plasma energy transports across the separatrix to the SOL, ion energy usually transports along magnetic field lines with lower thermal conduction than that for electrons, resulting in τ_u being larger than unity. Then the thermal energy could transfer from ions to electrons with the transfer rate satisfying

$$Q_{\rm eq} = \frac{3m_e}{m_i} n_e \nu_{\rm eq} \left(kT_i - kT_e \right) \tag{1}$$

where the temperature equilibration frequency satisfies

$$\nu_{eq} \approx 2.9 \times 10^{-12} n_e \ln \Lambda T_e^{-3/2}$$
. (2)

Larger value of $T_i - T_e$ and higher collisionality would increase the energy transfer rate, which results in an increase of the electron thermal energy. Consequently, τ_u gradually decreases with the increase of the plasma collisionality as the EDGE2D and onion-skin model simulations predicted [15]. This was also observed in experiments as seen in figure 12,

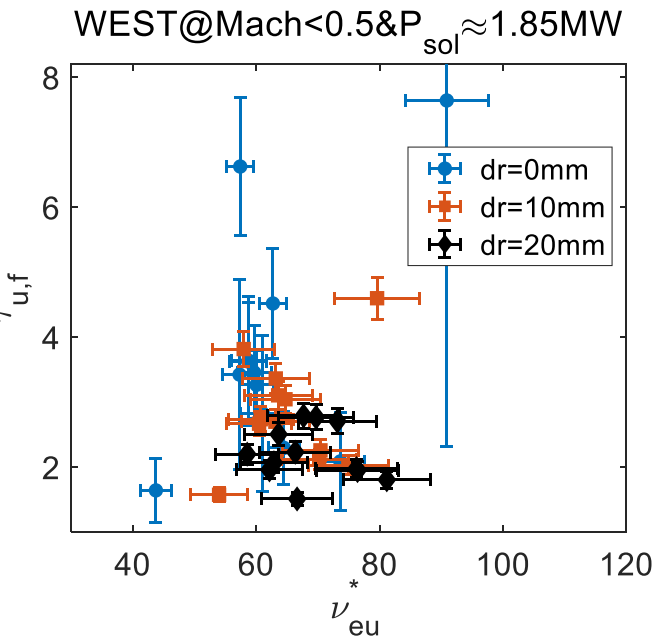


Figure 12. $\tau_{u,f}$ as a function of upstream normalized electron collisionality.

where $\tau_{u,f}$ gradually decreases from 4 to 2 as the upstream normalized electron collisionality $\nu_{\rm eu}^* = 10^{-16} n_{\rm eu} L_{\parallel}/T_{\rm eu}^2$ [15] increases from 60 to 80. L_{\parallel} in this formula is the magnetic connection length from the outboard midplane to divertor target and is roughly constant (\sim 45 m) when $dr \in (0,20)$ mm in this dataset. This relation seems also independent on the radial position of measurement which was changed from the separatrix to 20 mm further into the SOL. Note that some points for $\tau_u < 2$ and $\tau_u > 4$ are deviated from the $\tau_u(\nu_{\rm eu}^*)$ trends. This deviation may be because the value of $\tau_{u,f}$ is extraplotated but not measured.

After substituted the upstream plasma parameters into equation (1), $Q_{\rm eq}$ is estimated and shown in figure 13 as a function of $\nu_{\rm eu}^*$. Although that $Q_{\rm eq}$ is proportional with $\nu_{\rm eq} \propto \nu_{\rm eu}^*$, the relation of $Q_{\rm eq}$ with $\nu_{\rm eu}^*$ is also affected by the parameter of $T_i - T_e$ which causes $Q_{\rm eq}$ gradually decreases with the increase of $\nu_{\rm eu}^*$ near the separatrix. Further away from the separatrix, since the value of n_e and $T_i - T_e$ exponentially decay along the radial direction, $Q_{\rm eq}$ gradually decreases as the increase of dr, and increases with $\nu_{\rm eu}^*$ when the measurement position is 20 mm away from the separatrix.

In the SOL, assuming that there is no heat source and sink exist in the volume, the transferred energy between ions and electrons is mainly came from the perpendicular heat flux transport which could be estimated by the following equations:

$$Q_{\perp,i} = \nabla_{\perp} \cdot \vec{q}_{\perp}^{i} \tag{3.1}$$

$$Q_{\perp,e} = \nabla_{\perp} \cdot \vec{q}_{\perp}^{e} \tag{3.2}$$

where \vec{q}_{\perp}^{i} and \vec{q}_{\perp}^{e} are the ion and electron perpendicular heat flux, respectively. Substituting the terms of $\nabla_{\perp} = \frac{1}{r} \frac{\partial}{\partial r} r$,

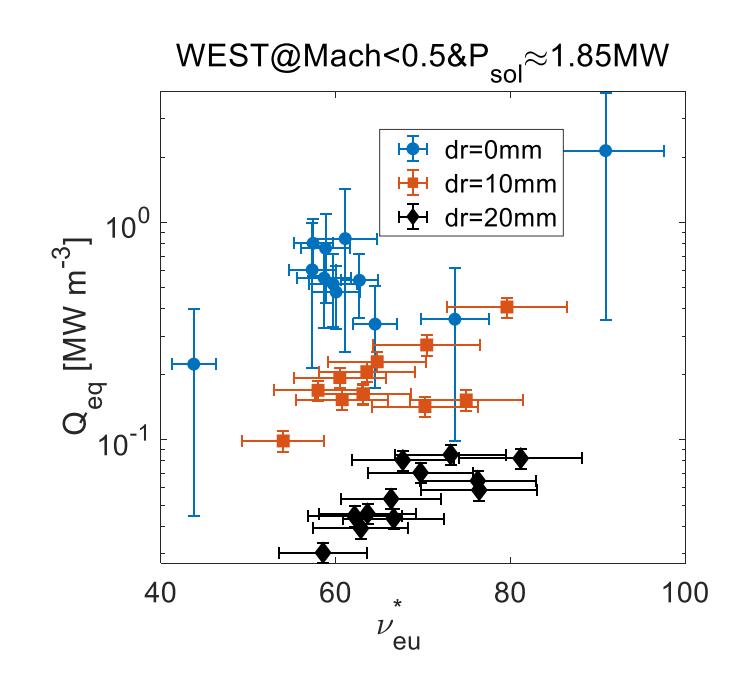


Figure 13. Upstream energy transfer rate between ions and electrons as a function of upstream normalized electron collisionality.

 $q_{\perp}^{i} = n\chi_{\perp}^{i} \frac{\partial(kT_{e})}{\partial r} + \frac{5}{2}kT_{i}D_{\perp} \frac{\partial n_{e}}{\partial r}, \quad q_{\perp}^{e} = n\chi_{\perp}^{e} \frac{\partial(kT_{e})}{\partial r} + \frac{5}{2}kT_{e}D_{\perp} \frac{\partial n_{e}}{\partial r}$ into equations (3.1) and (3.2) leads to

$$Q_{\perp,i} = \left(\frac{\chi_{\perp}^{i}}{\lambda_{\text{Ti}}} + \frac{5}{2} \frac{D_{\perp}}{\lambda_{\text{ne}}}\right) \frac{\partial P_{i}(r)}{\partial r}$$
(4.1)

$$Q_{\perp,e} = \left(\frac{\chi_{\perp}^{e}}{\lambda_{\text{Te}}} + \frac{5}{2} \frac{D_{\perp}}{\lambda_{\text{ne}}}\right) \frac{\partial P_{e}(r)}{\partial r}$$
(4.2)

where λ_{Ti} , λ_{Te} and λ_{ne} are the decay lengths of upstream ion and electron temperature and upstream electron density, respectively. The perpendicular ion and electron heat transport coefficients χ_{\perp}^{i} and χ_{\perp}^{e} are assumed to be equal to each other [15]. χ_{\perp}^{e} and the perpendicular particle transport coefficient D_{\perp} could be expressed as [15]

$$\chi_{\perp}^{e} \approx \frac{A_{\chi} \lambda_{\text{Te}}^{2}}{\nu_{\text{eu}}^{*}} \frac{C_{s}}{L_{\parallel}}$$
 (5)

$$D_{\perp} \approx \frac{\lambda_{\rm ne}^2}{2} \frac{C_s}{L_{||}} \tag{6}$$

Where $A_\chi = \frac{4}{49} \frac{10^{-16}}{e} \sqrt{\frac{m_i}{e}} \kappa_{0\rm e}$, $\kappa_{0\rm e} = \frac{30692}{Z_i {\rm ln} \Lambda}$, $C_s = \sqrt{T_e/m_i}$, Substituting equations (5) and (6) into equations (4.1) and (4.2), the perpendicular ion and electron energy rate, $Q_{\perp,i}$ and $Q_{\perp,e}$, are estimated. Figure 14 shows the estimation of χ^e_\perp and D_\perp based on equations (5) and (6), and $Q_{\perp,i}$ and $Q_{\perp,e}$ as a function of $Q_{\rm eq}$. λ_{Ti} for these 12 cases varies from 0.012 m to 0.037 m as shown in figure 10(b). The value variation of $\lambda_{\rm Te}$ and $\lambda_{\rm ne}$ are shown in figures 14(a) and (b). The calculated value of χ^e_\perp and D_\perp near the separatrix vary between [0.3 0.4] m² s⁻¹ and [0.1 0.3] m² s⁻¹, respectively. The result indicates that $Q_{\perp,i}$ and $Q_{\perp,e}$ are proportional with $Q_{\rm eq}$. And these trends are independent on the radial position

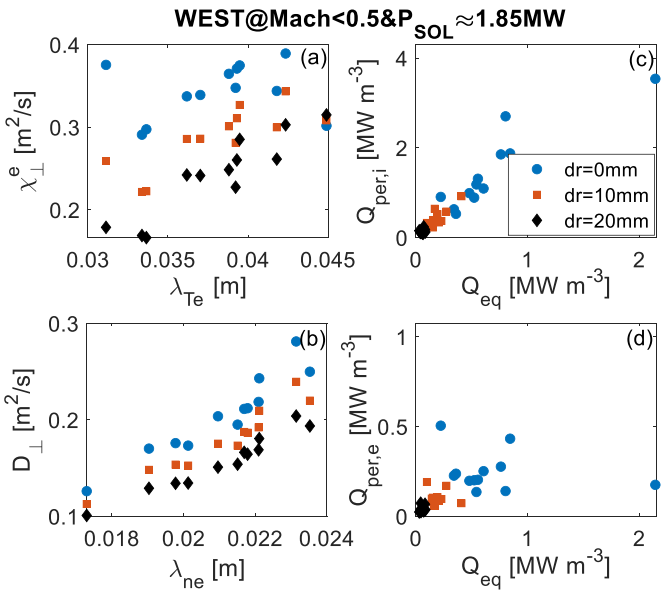


Figure 14. Relation of (a) χ_{-}^{e} with λ_{Te} , (b) D_{\perp} with λ_{ne} , upstream (c) ions and (d) electrons perpendicular energy transport rate as a function of upstream energy transfer rate from ions to electrons.

in the SOL. The ratios of $Q_{\rm eq}/Q_{\perp,i}$ and $Q_{\rm eq}/Q_{\perp,e}$ are roughly constant with the value of $Q_{\rm eq}/Q_{\perp,i}\sim 1/2$ and $Q_{\rm eq}/Q_{\perp,e}\sim 2$. These comparable values among $Q_{\rm eq}$, $Q_{\perp,i}$ and $Q_{\perp,e}$ imply that the energy transfer rate in the edge plasma energy balance play an important role and may even affect the downstream $T_{\rm id}/T_{\rm ed}$ ratio.

4.2. Dependence of divertor ion impact energy on upstream plasma parameters

Considering the ion and electron heat flux balance along the flux tube [15],

$$q_{\text{id},\parallel}A_{\parallel d} = q_{\text{iu},\parallel}A_{\parallel u} - \int_{d}^{u} (Q_{\text{eq}} + Q_{\text{Ei}})A_{\parallel}(s_{\parallel}) ds_{\parallel}$$
 (7.1)

$$q_{\text{ed},\parallel} A_{\parallel d} = q_{\text{eu},\parallel} A_{\parallel u} + \int_{d}^{u} \left(Q_{\text{eq}} - Q_{R}^{Z} - Q_{\text{Ee}} \right) A_{\parallel} \left(s_{\parallel} \right) ds_{\parallel}$$
(7.2)

where $q_{\mathrm{id},\parallel}$ and $q_{\mathrm{ed},\parallel}$ are the downstream ion and electron parallel heat flux, Q_{Ei} is the ion energy loss caused by ionization and charge exchanges with neutrals, Q_{Ee} is the electron cooling caused by neutrals, Q_R^Z is the electrons and impurities interaction, $A_{\parallel u}$ and $A_{\parallel d}$ are the upstream and downstream cross section area of the flux tube, respectively. Since $q_{\mathrm{ed},\parallel} = 5M_dkT_{\mathrm{ed}}n_{\mathrm{ed}}c_{\mathrm{sd}}$, $q_{\mathrm{id},\parallel} = \left(\frac{5}{2}kT_{\mathrm{id}} + \frac{1}{2}M_d^2\left(kT_{\mathrm{ed}} + kT_{\mathrm{id}}\right)\right)M_dn_{\mathrm{ed}}c_{\mathrm{sd}}$, where $c_{\mathrm{sd}} = \sqrt{\left(kT_{\mathrm{ed}} + kT_{\mathrm{id}}\right)/m_i}$, M_d is the downstream mach number, the downstream ion and electron temperature could be expressed to

$$\frac{3T_{\mathrm{id}} + 0.5T_{\mathrm{ed}}}{5T_{\mathrm{ed}}} = \frac{q_{\mathrm{iu},\parallel} A_{\parallel u} - \int_{d}^{u} (Q_{\mathrm{eq}} + Q_{\mathrm{E}i}) A_{\parallel} \left(s_{\parallel}\right) \mathrm{d}s_{\parallel}}{q_{\mathrm{eu},\parallel} A_{\parallel u} + \int_{d}^{u} (Q_{\mathrm{eq}} - Q_{R}^{\mathrm{Z}} - Q_{\mathrm{E}e}) A_{\parallel} \left(s_{\parallel}\right) \mathrm{d}s_{\parallel}}$$

where M_d has been assumed to be unity. When $T_{\rm ed}$ is still larger than 20 eV as shown in this paper, the power loss due to neutrals and impurities is still negligible [30]. Then equation (8) could be simplified to

$$\frac{3T_{\rm id} + 0.5T_{\rm ed}}{5T_{\rm ed}} \approx \frac{q_{\rm iu,\parallel} A_{\parallel u} - \int_{d}^{u} Q_{\rm eq} A_{\parallel} \left(s_{\parallel}\right) ds_{\parallel}}{q_{\rm eu,\parallel} A_{\parallel u} + \int_{d}^{u} Q_{\rm eq} A_{\parallel} \left(s_{\parallel}\right) ds_{\parallel}}$$
(9)

The above equation indicates that the downstream $T_{\rm id}/T_{\rm ed}$ ratio gradually decreases with the increase of $Q_{\rm eq}$. This implies that the energy transfer from ions to electrons along the flux tube has enhanced the downstream electron temperature, which would be further discussed in section 4.3. Because in the divertor region the downstream normalized electron collisionality $\nu_{\rm ed}^* = 10^{-16} n_{\rm ed} L_{\parallel}/T_{\rm ed}^2$ usually is larger than 100, electrons and ions are coupled with each other and leads the downstream $T_{\rm id}/T_{\rm ed}$ ratio to approach to unity based on extrapolating the τ_u ($\nu_{\rm eu}^*$) relation as shown in figure 12.

Combining equation (9) with the pressure balance along the flux tube,

$$2n_{\rm ed} (T_{\rm id} + T_{\rm ed}) = n_{\rm eu} (T_{\rm iu} + T_{\rm eu})$$
 (10)

the downstream ion impact energy E_i could be deduced to

$$E_{i} = \varepsilon \frac{n_{\text{eu}}}{n_{\text{ed}}} T_{\text{eu}} \left(1 + \tau_{u} \right) \tag{11}$$

Where $\varepsilon = \left(1 + \frac{3}{5+10\alpha}\right)$ and $\alpha \approx \frac{q_{\mathrm{iu},\parallel}A_{\parallel u} - \int_{u}^{u}Q_{\mathrm{eq}}A_{\parallel}\left(s_{\parallel}\right)\mathrm{d}s_{\parallel}}{q_{\mathrm{eu},\parallel}A_{\parallel u} + \int_{u}^{u}Q_{\mathrm{eq}}A_{\parallel}\left(s_{\parallel}\right)\mathrm{d}s_{\parallel}}$. Equation (11) indicates that the ion impact energy near the target is proportional with the upstream T_{eu} and τ_{u} . The energy transfer from ions to electrons directly affect the coefficient ε . Increasing Q_{eq} along the flux tube would gradually decrease α , which in turn gradually increases E_{i} . Since $T_{\mathrm{eu}} \approx \left(\frac{7P_{\mathrm{SoL}}\hat{q}_{\mathrm{cyl}}^{2}A}{16\kappa_{0}^{c}\hat{k}\lambda_{q}}\right)^{2/7}$ [31], equation (11) could be changed to

$$E_{i} = \varepsilon \frac{n_{\text{eu}}}{n_{\text{ed}}} \left(\frac{7P_{\text{SOL}}\hat{q}_{\text{cyl}}^{2}A}{16\kappa_{o}^{e}\hat{k}\lambda_{a}} \right)^{2/7} (1 + \tau_{u})$$
 (12)

where the aspect ratio A=R/a, $\hat{\kappa}=\sqrt{\frac{1+\kappa_{\rm geo}^2(1+2\delta^2-1.2\delta^3)}{2}}$, $\kappa_{\rm geo}$ is the elongation, δ is the plasma triangularity, $\hat{q}_{\rm cyl}=\frac{B_{\rm tor}}{B_{\rm pol}}\cdot\frac{\hat{\kappa}}{A}$ with $B_{\rm pol}=\frac{\mu_0 I_p}{2\pi a\hat{\kappa}}$, the parallel heat constant $\kappa_0^e=\frac{2000}{f_{\kappa,0}(Z_{\rm eff})}\frac{W}{(eV)^{7/2}m}$ with $f_{\kappa,0}(Z_{\rm eff})=0.672+0.076Z_{\rm eff}^{0.5}+0.252Z_{\rm eff}$. λ_q is the power width in the SOL. Its scaling has been proposed in different expressions [32, 33]. For almost constant $P_{\rm SOL}$ and magnetic geometry as shown in this paper, increasing $n_{\rm eu}$ was observed to significantly decrease τ_u and slightly increase $T_{\rm eu}$ due to the energy transfer from ions to electrons. As a result, $Y_{\rm W}$ in figure 11 gradually decreases with $T_{\rm eu}$.

4.3. Estimation of upstream and downstream electron temperature ratio

For a simple SOL model, the upstream and downstream electron temperature ratio, $f_t = T_{\text{eu}}/T_{\text{ed}}$, satisfies follows as shown in [15].

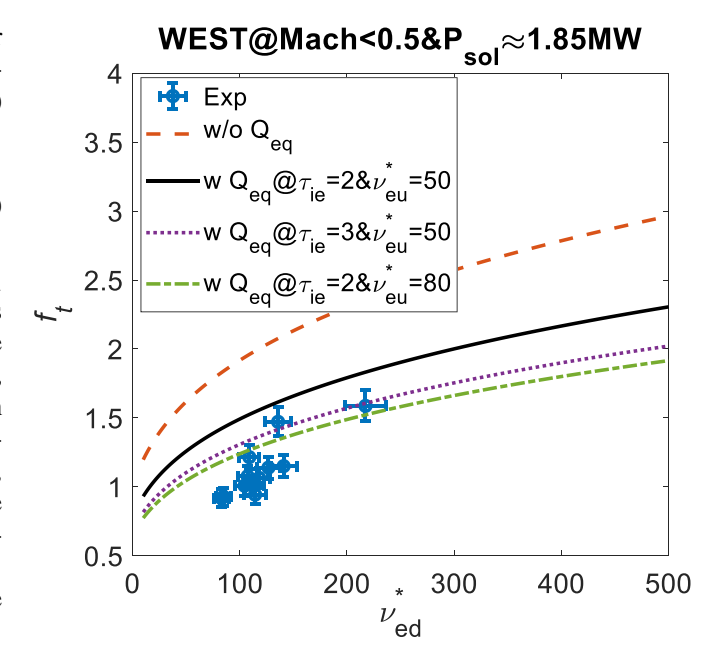


Figure 15. f_t as a function of the downstream normalized electron collisionality.

$$f_t^{7/2} - 1 = \frac{n_t L_{\parallel}}{C_1 T_{\text{ad}}^2} \tag{13}$$

where $C_1 = \frac{2\kappa_e}{7\gamma e C_{s0}} \sim 10^{17}$, the sheath heat transmission coefficient $\gamma \approx 7$ and $C_{s0} = \sqrt{\frac{2}{m_i}}$. Then the right hand of equation (13) satisfies $\frac{n_t L_{\parallel}}{C_1 T_{\rm ed}^2} = \frac{\nu_{\rm ed}^*}{C_1 10^{-16}} \sim \frac{\nu_{\rm ed}^*}{10}$. Substituting them into equation (13) obtains f_t

$$f_t = \left(\frac{\nu_{\rm ed}^*}{C_1 10^{-16}} + 1\right)^{2/7}.$$
 (14)

When the ion and electron energy exchange is introduced, based on the two-point model including the ion temperature [20], the f_t equation could be extended to

$$f_t^{7/2} - 1 = \frac{n_t L_{\parallel}}{C_1 T_{\text{ed}}^2} - \frac{7Q_{eq} L_{\parallel}^2}{4\kappa_e T_{ed}^{7/2}}.$$
 (15)

Then equation (14) is changed to

$$f_t = \left(\frac{\frac{\nu_{ed}^*}{C_1 10^{-16}} + 1}{1 + C_2 (\tau_u - 1) \nu_{eu}^{*2}}\right)^{2/7}$$
(16)

where $C_2 = \frac{42 \times 10^{16} e(2em_e)}{8.8 \kappa_e m_i}^{1/2}$. Equation (16) indicates that the introduced energy transfer term $C_2 (\tau_u - 1) \nu_{\rm eu}^{*2}$ would reduce f_t , i.e. enhance the downstream electron temperature.

In experiments, the measured f_t is observed to gradually increase from ~ 1 to ~ 1.5 as $\nu_{\rm ed}^*$ increases from 100 to 200. Comparing with the theoretical calculation by equation (14), the measured f_t is only half as shown in figure 15. When considering the energy transfer term from ions to electrons, the

predicated f_t by equation (16) is much closer to the measurement point. Note that the energy transfer term is scanned by changing the parameters of τ_u and $\nu_{\rm eu}^*$ in equation (16).

5. Conclusion

This paper studies the influence of ion temperature in the SOL to the divertor W sputtering in the WEST tokamak. The measured WI emission reflects the gross W erosion. The net W source which includes the prompt redeposition of W has not been considered in the studies presented here. The covered parameter space in divertor electron density and temperature in the present study is limited and only very moderate variation of the re-deposition factor is considered [17], which is not hampering the main correlation. The T_{iu} and downstream plasma parameters are varied by changing the upstream electron density and maintaining a constant SOL power under a lower hybrid wave heating plasma. The W sputtering yield was observed to gradually increase with $T_{iu,f}$ and $\tau_{u,f}$, while decreased with T_{eu} , where $T_{iu,f}$ is extrapolated by exponentially fitting the RFA measurement. This phenomenon is attributed to the energy transfer between ions and electrons in the SOL. Its value comparing with the perpendicular ion and electron energy transport rates are roughly $Q_{\rm eq}/Q_{\perp,i} \sim 1/2$ and $Q_{\rm eq}/Q_{\perp,e}\sim 2$. This indicates that the energy transfer from ions to electrons plays an important role in governing the edge plasma energy balance.

An theoretical analysis indicates that the divertor ion impact energy is proportional to $T_{\rm eu}(1+\tau_u)$ and could be enhanced by the increase of Q_{eq} along the flux tube when the power loss due to neutrals and impurities is still negligible. An analytical equation considering the ion and electron coupling term is introduced to predict the upstream and downstream electron temperature ratio $(T_{\rm eu}/T_{\rm ed})$. The result is more precise than the traditional analytical equation in comparing with the experimental measurement. Based on the new analytical equation, $Q_{\rm eq}$ plays a significant role to enhance the downstream T_{ed} and potentially increase the W material sputtering risk. This work may help to facilitate the understanding of the effect of the coupled ion and electron energy on the W sputtering.

Acknowledgments

The authors deeply appreciate the continued research and operational efforts of the entire WEST team. Author Y. Li appreciates J.P. Gunn and C. Guillemaut for the help to get access to the WEST probe and visible spectroscopy data, respectively, and A. Thierry, D. Moulton, X. Liu, X.Q. Wu, S.Y. Dai and F. Ding for valuable discussions, Jonathan Gaspar for providing the divertor infrared camera and thermal couple data and D. O'Mullane for providing the SXB data. This work has been carried out within the framework of the EUROfusion Consortium and has received funding from the Euratom research and training programme 2014-2018 and 2019-2020 under Grant Agreement No. 633053. The views and opinions expressed herein do not necessarily reflect those of the European Commission. The research was also supported by the International Postdoctoral Exchange Fellowship Program under Grant 20170009 and the National Natural Science Foundation of China under Grant 11705237.

ORCID iDs

Y. Li https://orcid.org/0000-0001-8008-1880 G.S. Xu https://orcid.org/0000-0001-8495-8678 S. Brezinsek https://orcid.org/0000-0002-7213-3326 J. Morales https://orcid.org/0000-0002-3140-0504

References

- [1] ITER Physics Basis Editors et al 1999 Nucl. Fusion 39 2137
- [2] Matthews G.F. et al 2011 Phys. Scr. T145 014001
- [3] Neu R. et al 2011 J. Nucl. Mater. 415 \$322
- [4] Bucalossi J. et al 2014 Fusion Eng. Des. 89 907
- [5] Philipps V., Roth J. and Loarte A. 2003 Plasma Phys. Control. Fusion 45 A17
- [6] Brezinsek S. 2015 J. Nucl. Mater. 463 11
- [7] Federici G. et al 2001 Nucl. Fusion 41 1967
- Brezinsek S. et al 2019 Nucl. Fusion 59 096035
- Kallenbach A. et al 2011 J. Nucl. Mater. 415 S19
- [10] Dux R. et al 2009 J. Nucl. Mater. 390-391 858
- Guillemaut C. et al 2015 Plasma Phys. Control. Fusion **57** 085006
- [12] Fedorczak N. et al 2015 J. Nucl. Mater. 463 85
- [13] Den Harder N. et al 2016 Nucl. Fusion 56 026014
- [14] Huber A. et al 2020 Nucl. Mater. Energy 25 100859
- [15] Stangeby P.C. 2000 The Plasma Boundary of Magnetic Fusion Devices (Boca Raton, FL: CRC Press)
- [16] Guillemaut C. et al 2016 Phys. Scr. T167 014005
- [17] Kirschner A., Tskhakaya D., Brezinsek S., Borodin D., Romazanov J., Ding R., Eksaeva A. and Linsmeier C. 2018 Plasma Phys. Control. Fusion 60 014041
- [18] Kočan M., Gunn J.P., Pascal J.Y., Bonhomme G., Fenzi C., Gauthier E. and Segui J.L. 2008 Plasma Phys. Control. Fusion 50 125009
- [19] Elmore S. et al 2012 Plasma Phys. Control. Fusion 54 065001
- [20] Li Y. et al 2019 Nucl. Fusion 59 126002
- [21] Li Y. et al 2022 Nucl. Fusion 62 094002
- [22] Bucalossi J. 2009 Fusion Sci. Technol. **56** 1366
- [23] Kočan M., Gunn J.P., Komm M., Pascal J.Y., Gauthier E. and Bonhomme G. 2008 Rev. Sci. Instrum. 79 073502
- [24] Dejarnac R., Sestak D., Gunn J.P., Firdaouss M., Greuner H., Pascal J.Y., Richou M. and Roche H. 2021 Fusion Eng. Des. 163 112120
- [25] Meyer O. et al 2018 Rev. Sci. Instrum. 89 10D105
- [26] Faugeras B. 2020 Fusion Eng. Des. 160 112020
- [27] Brezinsek S. et al 2017 Phys. Scr. 2017 014052
- [28] Di Genova S. et al 2021 Nucl. Fusion 61 106019
- [29] Erents S.K., Stangeby P.C., LaBombard B., Elder J.D. and Fundamenski W. 2000 Nucl. Fusion 40 295
- [30] Stangeby P.C. 2018 Plasma Phys. Control. Fusion 60 044022
- [31] Eich T., Manz P., Goldston R.J., Hennequin P., David P., Faitsch M., Kurzan B., Sieglin B. and Wolfrum E. 2020 Nucl. Fusion 60 056016
- [32] Eich T. et al 2013 Nucl. Fusion 53 093031
- [33] Liu X., Nielsen A.H., Rasmussen J.J., Naulin V., Wang L., Ding R. and Li J. 2022 Nucl. Fusion 62 076022